Materials Today Bio 15 (2022) 100279

Contents lists available at ScienceDirect

Materials Today Bio

journal homepage: www.journals.elsevier.com/materials-today-bio

Erythrocyte membrane-camouflaged nanoparticles as effective and biocompatible platform: Either autologous or allogeneic erythrocyte-derived

Jun Dai [a], Zhaojun Chen [b], Shixuan Wang [a], Fan Xia [b], Xiaoding Lou [b,*]

[a] Department of Obstetrics and Gynecology, Tongji Hospital, Tongji Medical College, Huazhong University of Science and Technology, Wuhan, 430030, China
[b] State Key Laboratory of Biogeology and Environmental Geology, Faculty of Materials Science and Chemistry, China University of Geosciences, Wuhan, 430074, China

ARTICLE INFO

Keywords:
Biomimetic nanoparticles
Erythrocyte
Aggregation-induced emission
Photodynamic therapy
Safety assessment

ABSTRACT

Erythrocytes are often used for the development of cell membrane camouflaged nanoparticles (NPs) due to their wide range of sources. However, whether the difference between autologous and allogeneic sources for the erythrocyte membranes have an influence on the performance of camouflaged NPs, which is still inconclusive. To this end, we developed two aggregation-induced emission (AIE) photosensitizers camouflaged with erythrocyte membranes (E-M), named E-M_{auto}@P and E-M_{allo}@P, which were prepared using autologous- and allogeneic-derived erythrocytes, respectively. In vivo, E-M@P-mediated photodynamic therapy (PDT) effectively inhibited tumor growth, and this therapeutic effect did not differ between E-M_{auto}@P and E-M_{allo}@P. Importantly, there were no differences between E-M_{auto}@P and E-M_{allo}@P treated mice in terms of general condition, organ function or immune system. Both E-M_{auto}@P and E-M_{allo}@P have been shown not to cross the placental barrier and do not affect the development of the embryo, which could be a good platform for the treatment of pregnancy-related disorders. These findings provided more detailed evidences for erythrocyte membrane camouflaged NPs as a promising therapeutic platform, since there is no difference in efficacy or biosafety of either autologous or allogeneic erythrocyte-derived NPs.

1. Introduction

Obtaining good therapeutic effect is the goal that biomaterials should pursue, but we often ignore the preconditions for their application in vivo, that is, their biocompatibility and biosafety [1,2]. The exogenous nature makes synthetic biomaterials prone to trigger passive immune clearance mechanisms and increase reticuloendothelial system clearance effects, leading to their low bioavailability [3,4]. At the same time, these synthetic biomaterials may also have serious toxic side effects that severely limit its application in vivo [5–7]. In contrast, natural biomaterials are less likely to trigger an immune response in the body and have a higher biosafety profile [8–10]. Recently, a cell membrane cloaking technique has been reported as a novel interfacing approach, and proved useful for improving the performance of synthetic biomaterials [11–14]. The use of cell membrane camouflaged nanoparticles (NPs) has resulted in the acquisition of natural physicochemical properties on the cell membrane, including proteins, lipids, glycoproteins et al., thus allowing the NPs to inherit their unique biological functions [15–17]. The derived biological properties and functions, such as immunosuppressive ability, long circulation capacity and target recognition, could enhance their potential for medical applications.

With the development of cell membrane cloaking technology, more and more types of cells are being developed, such as erythrocytes [18–21], platelets [22,23], macrophages [24,25], tumor cells [26–30] and stem cells [31,32]. Among them, erythrocytes, also known as red blood cells, are a natural biomaterial with a wide range of sources. The earliest development of cell membrane cloaking technology was the construction of cell membrane camouflaged NPs by co-extrusion using erythrocyte membrane as the outer membrane and polymer as the nanocore [33]. This erythrocyte membrane camouflaged NPs have superior circulation ability in vivo than traditional synthetic materials such as polyethylene glycol (PEG). Since then, there has been an increasing number of cell membrane cloaking technology developments based on erythrocyte membranes, with applications in a variety of fields [34–40]. Zhang's group used erythrocyte membranes to construct a detoxifiable nanosponge that effectively avoids hemolysis mediated by pore-forming toxins [41]. Further, Green and co-workers obtained better in vivo circulation properties of erythrocyte membrane camouflaged NPs by altering the nanocore traits to achieve more efficient toxins detoxification [42]. In addition to detoxification, erythrocyte membrane

* Corresponding author.
E-mail address: louxiaoding@cug.edu.cn (X. Lou).

https://doi.org/10.1016/j.mtbio.2022.100279
Received 22 February 2022; Received in revised form 22 April 2022; Accepted 2 May 2022
Available online 5 May 2022

camouflaged NPs have potential in the field of tumor diagnosis and treatment [43–45]. The spleen is the site of removal of damaged or senescent red blood cells, called the homing effect [46]. Using this feature, immune adjuvants loaded in erythrocyte membrane camouflage NPs can be actively delivered to the spleen to activate the body's anti-tumor immunity [47]. Moreover, the erythrocyte membrane camouflaged NPs have good ERP effect and can effectively target the delivery of drugs or therapeutic components to tumors [48,49]. Erythrocyte membrane-based camouflage technology has also been addressed in the fields of antimicrobial [50]. Despite the exciting advancements, the research of biosafety for erythrocyte membrane camouflaged NPs is still in a nascent stage. The research on how to choose and utilize the erythrocyte membrane with wide resources is significant, since the working environment for camouflaged NPs is unknown and complex.

To explore the differences in the effectiveness and safety of erythrocyte membrane camouflaged NPs, we constructed two NPs, E-M_{auto}@P and E-M_{allo}@P. E-M_{auto}@P used autologous-derived erythrocytes for the preparation of erythrocyte membrane camouflage NPs, while E-M_{allo}@P used allogeneic-derived erythrocytes, both of which have aggregation-induced emission luminogens (AIEgens) and poly lactic-*co*-glycolic acid (PLGA) complex in their nanocore (Scheme 1). Due to the good fluorescence properties and photosensitivity of AIEgens (PF3-PPh_3), it enables tracing of erythrocyte membrane camouflaged NPs and photodynamic therapy (PDT) of tumors. In vitro and in vivo, we confirmed that both E-M_{auto}@P and E-M_{allo}@P effectively inhibit tumor growth, and there was no difference in efficiency between them. More importantly, we also found that both E-M_{auto}@P and E-M_{allo}@P have good biocompatibility and do not trigger immune responses in the body. Also, E-M_{auto}@P and E-M_{allo}@P have good safety profile in pregnant mice. These findings suggested that either autologous or allogeneic erythrocyte are ideal materials for preparing erythrocyte membrane camouflage NPs.

2. Results and discussion

The construction of cell membrane camouflaged NPs usually requires a stable nanocore that is generally composed of functional molecules and scaffold components [51–55]. Here, we used the AIEgen (PF3-PPh_3) as a functional molecule (Figure S1-S2), since they not only possess high fluorescence quantum yields and resistance to photobleaching, but also have photodynamic therapy effect [47,56–58]. To construct a stable nanocore, PLGA was used as a scaffold to mix with PF3-PPh_3. Then, by co-extruding erythrocyte membrane (E-M) and PLGA/PF3-PPh_3 (P) nanocore, erythrocyte membrane camouflaged NPs (E-M@P) were obtained. Dynamic light scattering (DLS) and transmission electron microscopy (TEM) showed that the particle size of E-M@P was around 200 nm (Fig. 1A). An envelope about 10 nm thick could be observed at the outer layer of NPs, proving the successful coating of erythrocyte membrane [41]. No significant change in the size of the E-M@P in PBS and 20% serum solutions were found within 12 days, indicating its good stability (Figure S3A). Moreover, E-M@P displayed the similar ultraviolet–visible (UV–vis) absorption spectra with PF3-PPh_3 (Figure S3B). The fluorescence intensity of E-M@P was higher than that of PF3-PPh_3 at the same concentration of PF3-PPh_3 (Fig. 1B), demonstrating that the membrane encapsulation enabled a tighter aggregation state [47]. The encapsulation of PF3-PPh_3 with cell membranes also offers additional advantages. Firstly, the anti-photobleaching performance of PF3-PPh_3 was improved, as reflected by the fact that the fluorescence intensity of PF3-PPh_3 was only 57.4% of the original one after 20 min of light exposure, while E-M@P was still 80.7% (Figure S3C) [59–62]. Secondly, the photosensitivity of PF3-PPh_3 was substantially enhanced after it was prepared as cell membrane camouflaged NPs by using 9,10-Anthracenediyl-bis(methylene)dimalonic Acid (ABDA) as an indicator of reactive oxygen species (ROS) (Fig. 1C) [63–65]. These results fully indicated that E-M@P was successfully prepared and after coating, the stability,

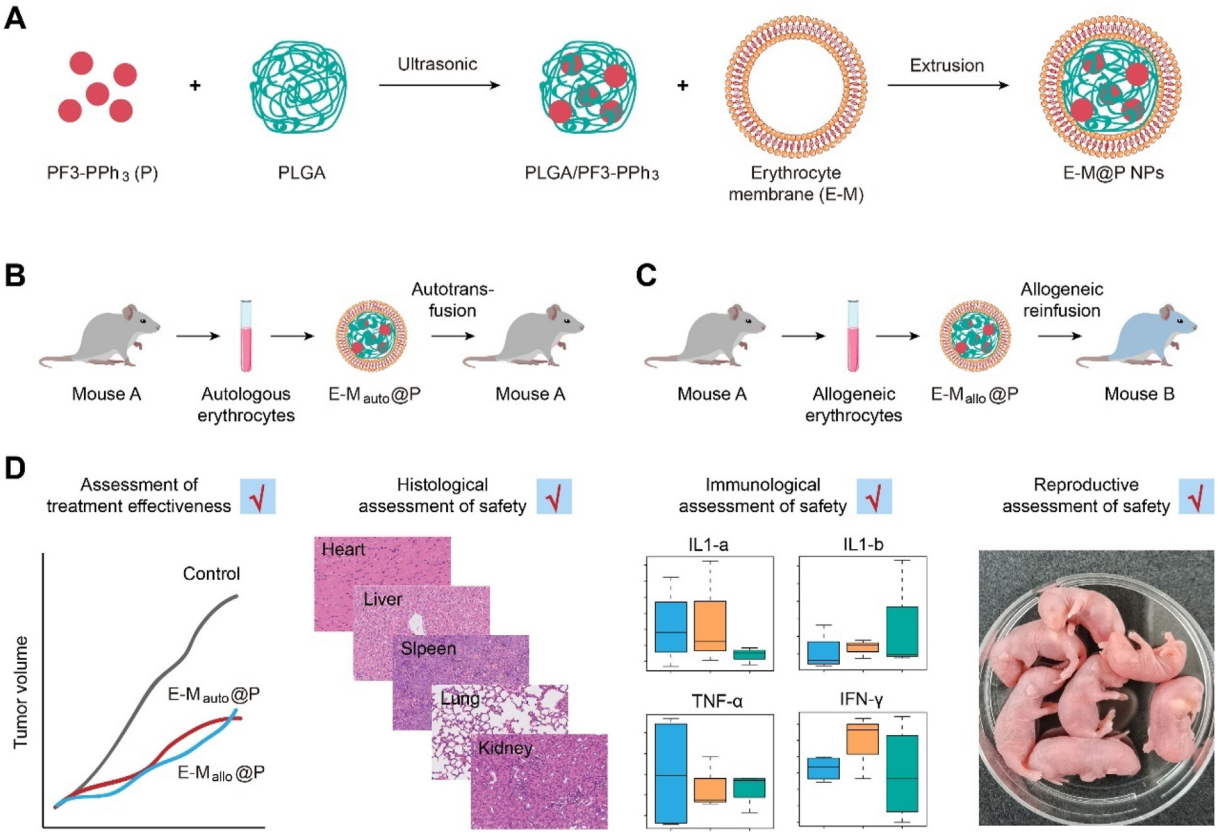

Scheme 1. (A) Preparation process of E-M@P NPs. (B) Schematic diagram of the use of (A) E-M_{auto}@P or (B) E-M_{allo}@P for the treatment of tumor-bearing mice. (C) Comparison of treatment efficiency and safety of E-M_{auto}@P and E-M_{allo}@P.

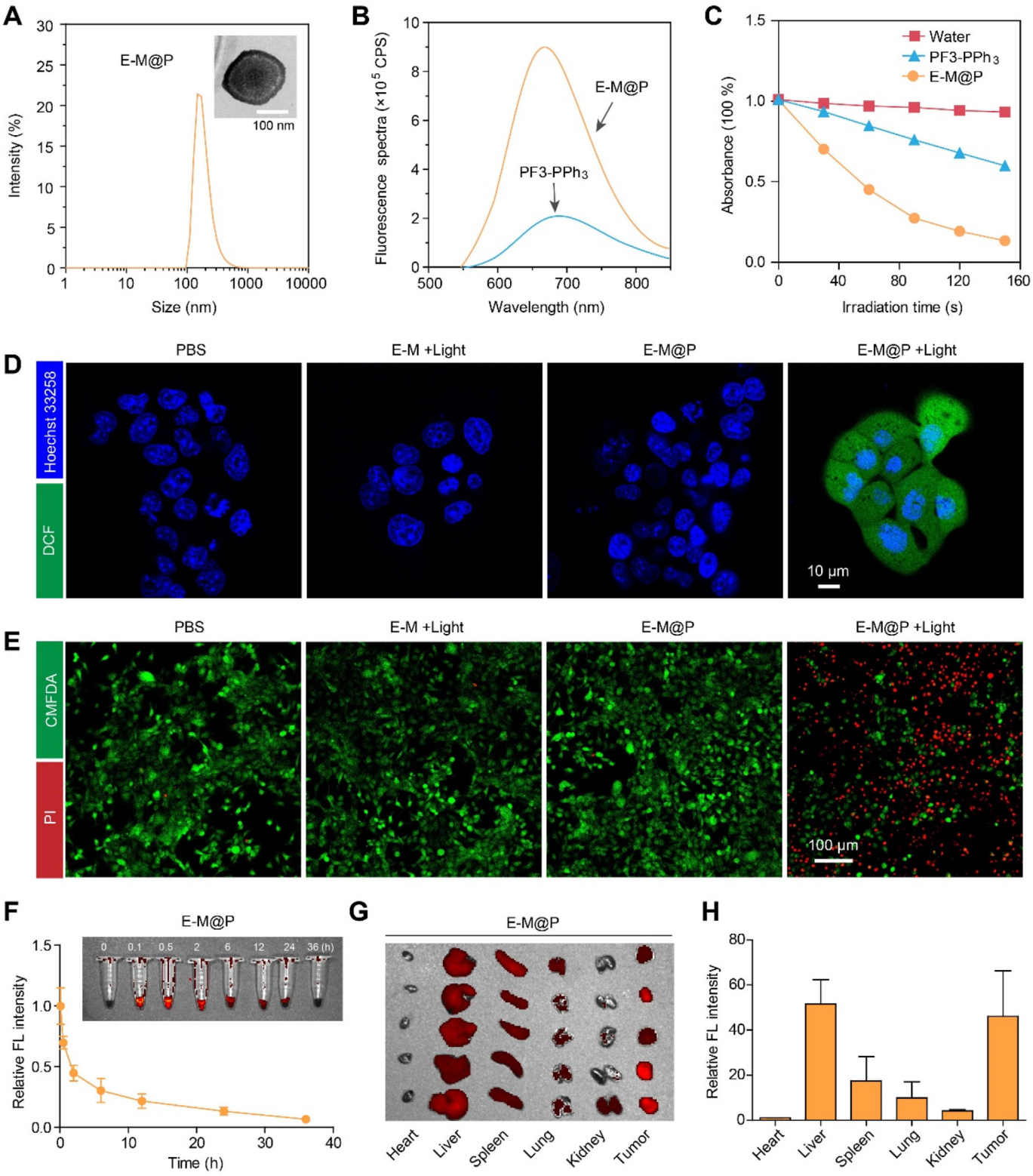

Fig. 1. Characterization of erythrocyte membrane camouflage NPs and evaluation of photodynamic therapeutic effects in vitro, as well as circulation kinetics and bio-distribution of E-M@P. (A) Hydrodynamic size distribution and TEM image of E-M@P. Scale bar = 100 nm. (B) Fluorescence spectra of PF3-PPh_3 and E-M@P. The concentration of PF3-PPh_3 is 10 μg/mL. (C) Photosensitivity of PF3-PPh_3 and E-M@P. The concentration of PF3-PPh_3 is 25 μg/mL. The concentration of ABDA is 50 μM. Light intensity is 100 mW cm^{-2}. (D) DCFH-DA detects the level of intracellular ROS. Light intensity: 100 mW cm^{-2}. Irradiation time: 3 min. DCFH-DA: Ex = 488 nm; Em = 540 nm. Hoechset 33,258: Ex = 350 nm, Em = 460 nm. (E) PI and CMFDA co-staining assays detect the viability of 4T1 cells after receiving PDT. Light intensity: 100 mW cm^{-2}. Irradiation time: 5 min. PI: Ex = 633 nm; Em = 660 nm. CMFDA: Ex = 488 nm; Em = 540 nm. The data were reported as mean ± SD and analyzed by two-sided Student's t-test. *$p < 0.05$, **$p < 0.01$, ***$p < 0.001$, n. s. not significant. (F) Circulation kinetics of E-M@P in mice. (G) Bio-distribution of E-M@P in a tumor-bearing mouse model. E-M@P: Ex = 500 nm, Em = 660 nm. (H) Quantitative analysis of E-M@P in tumor, liver, heart, spleen, lung and kidney.

photostability as well as photosensitivity were enhanced.

Then, the cell behaviors of E-M@P in vitro were in investigated. From the confocal laser scanning microscopy (CLSM) images (Figure S4), it could be clarified that E-M@P can be taken up by 4T1 cells (a mouse mammary cancer cell line) and the internalization amounts of E-M@P were positively correlated with its concentration (Figure S5). To compare the uptake of E-M@P in different cells, 4T1, HLF (lung fibroblasts), 293 T (human renal epithelial cells) and hESC (human endometrial mesenchymal cells) cell lines were used as test subjects. Quantitative fluorescence analysis showed that tumor cells 4T1 took up significantly more E-M@P than other normal cells, including HLF, 293 T and hESC cells (Figure S6-S7), demonstrating that it is promising in minimizing the toxic effects in vivo. The obvious uptake difference may be because normal cells have lower metabolic activity and therefore need to take up less external nutrients. Cell Counting Kit-8 (CCK-8) results showed that E-M@P were biocompatible with both tumor cells (4T1) and normal cells (293 T) in the absence of light, reflecting that NPs had no significant effect on cell viability in a certain concentration range (PF3-PPh_3 0–20 μg/mL) (Figure S8). Meanwhile, we further examined the effect of E-M@P on the viability of 4T1 and 293 T cells using live/dead cell double fluorescence staining (Figure S9). However, in the presence of light, E-M@P becomes a potent cell-killing agent due to the high-efficient ROS generation ability of AIEgen, which was also confirmed by the intracellular ROS indicator 2′-7′dichlorofluorescin diacetate (DCFH-DA) (Fig. 2D). Next, the propidium iodide (PI) and 5-chloromethylfluorescein diacetate (CMFDA) co-staining results also proved that tumor cells were killed only when both E-M@P and light irradiation conditions were present (Fig. 2E and Figure S10-S11). These results suggest that E-M@P has low dark toxicity and high phototoxicity towards tumor cells.

For biomaterials, whether it can be injected in vivo or not, it's hemolytic property should be tested first. Generally, it is considered safe if the hemolysis is less than 5% and can be used for intravenous injection [66]. Using water as a positive control group (hemolysis rate 100%), it was found that PF3-PPh_3 displayed a high hemolysis rate of 12.37%. While, after coating with erythrocyte membranes, the hemolysis rate decreased significantly to 2.53%, indicating that E-M@P can be used for intravenous injection (Figure S12). Next, the circulatory kinetics of E-M@P in vivo were investigated. As shown in Fig. 2F, E-M@P circulates in the body for more than 24 h, allowing it to passively target tumors through enhanced permeability and retention (EPR) effect [67]. In a mouse tumor model, E-M@P was injected into the mice through the tail vein and the tumor and organs were separated after 24 h. The distribution of E-M@P in tumors and organs was examined by In Vivo Imaging Systems (IVIS), and it was found that the tissues with the highest accumulation of NPs were liver and tumors, followed by spleen, lung, kidney and liver (Fig. 3G/H). The results demonstrated that E-M@P had long circulation kinetics and good passive tumor targeting ability for drug delivery to tumors.

To investigate the in vivo anti-tumour effects of nanoparticles constructed from erythrocyte membrane sources, two types of erythrocyte membrane camouflaged NPs, E-M_{auto}@P (autologous erythrocytes) and E-M_{allo}@P (allogeneic erythrocytes), were constructed. The therapeutic protocol of autologous erythrocyte membrane camouflaged NPs was shown in Fig. 2A, where NPs prepared from blood collected from “mouse A″ were used for tumor treatment of “mouse A”. While, when blood was collected from “mouse A″, and then “mouse B″ was treated. This was regarded as allogeneic erythrocyte membrane camouflaged NPs therapy (Fig. 2B). 4T1 tumor cells were inoculated into the right axilla of female Balb/c mice, and the tumors were randomly divided into the following three groups PBS, E-M_{auto}@P and E-M_{allo}@P when the tumors grew to about 80 mm^3. All mice were treated with light. At the end of the treatment, the tumors were removed from the mice and presented in Fig. 2C. The growth kinetic curves of these tumors in mice were shown in Fig. 2D. From the above results, it was found that either E-M_{auto}@P or E-M_{allo}@P -mediated PDT significantly inhibited tumor growth, and there was no difference in the inhibition efficiency between them both. There was also no significant difference in body weight change between PBS, E-M_{auto}@P and E-M_{allo}@P during treatment, implying good biocompatibility for both E-M_{auto}@P and E-M_{allo}@P (Fig. 2E). The mechanisms of E-M_{auto}@P and E-M_{allo}@P -mediated PDT inhibition of tumors were further investigated at the tissue and molecular levels. Hematoxylin-eosin (H&E) staining suggested that either E-M_{auto}@P and E-M_{allo}@P -mediated PDT caused necrosis of tumor tissues, as reflected by sparse arrangement of tumor tissues, disruption of cell morphology and coagulation or disappearance of nuclei in the E-M_{auto}@P and E-M_{allo}@P groups (Fig. 2F). At the molecular level, it was also confirmed by TdT-mediated dUTP nick end labeling (TUNEL) staining that tumors in the E-M_{auto}@P and E-M_{allo}@P groups showed a large number of apoptotic tumor cells (Fig. 2G). Ki-67 is a protein that reflects the state of cell proliferation. The expression of Ki-67 in tumors was detected by immunofluorescence staining. It was found that the proportion of tumor cells with positive expression of Ki-67 in PBS group was higher than that in E-M_{auto}@P and E-M_{allo}@P groups, which means that the proliferation of tumors in E-M_{auto}@P and E-M_{allo}@P groups was slower (Fig. 2H). These tests responding to the killing performance of PDT, including H&E, TUNEL and Ki-67 staining were not significantly different between E-M_{auto}@P and E-M_{allo}@P. In addition to direct killing of tumor cells, PDT has the role of assisting in enhancing immunotherapy and destroying blood vessels [68–71]. Here, PDT mediated by E-M_{auto}@P or E-M_{allo}@P is also able to promote $CD4^+$ and $CD8^+$ T cell chemotaxis and infiltration towards the tumor (Fig. 4I). Also, E-M_{auto}@P or E-M_{allo}@P -mediated PDT are able to destroy microvessels within the tumor (Fig. 2J). These results imply a potential application of E-M@P -mediated PDT in assisting the enhancement of antitumor immunotherapy and anti-vascular therapy. In this section, we illustrated that erythrocyte membrane camouflage NPs have similar antitumor effects and mechanisms whether they are derived from autologous or allogeneic erythrocytes.

To further confirm the biosafety of E-M@P, a set of animal experiments parallel to the tumor treatment was used. Healthy 8-week-old Balb/c mice were used for in vivo safety assessment by tail vein injection of PBS, E-M_{auto}@P and E-M_{allo}@P. As shown in Fig. 3A, the NPs prepared from blood obtained from “mouse A″ are reinfused back into “mouse A″, which is called autologous reinfusion. On the contrary, the NPs prepared from the blood obtained from “mouse A″ are reinfused back into “mouse B″, which is called allogeneic reinfusion. All mice showed no significant difference in diet and water intake during NPs injection, and no abnormal activities including tearing, screaming, scratching, and depression (Fig. 3B). Body weight changes of mice in all groups were also not significantly different during NPs infusion (Fig. 3C). Blood tests in mice suggested no difference in the number of erythrocytes, leukocytes and platelets after E-M_{auto}@P and E-M_{allo}@P injections, respectively (Fig. 3D). Next, the relative organ weights (Fig. 5E), histological (Fig. 3F) and biochemical markers (Fig. 3G) of the organs of the mice that received the different treatments were analyzed. First, the relative weights of the organs were analyzed and, as shown in Fig. 3E, were not different from both E-M_{auto}@P and E-M_{allo}@P compared to the PBS-injected group, and were not significantly different between E-M_{auto}@P and E-M_{allo}@P. Then, the morphological changes of the organs were analyzed by H&E staining. As shown in Fig. 3F, there was no significant difference in the morphology of all organs between the PBS, E-M_{auto}@P and E-M_{allo}@P groups. Finally, a series of biochemical parameters were tested to assess organ function. Albumin (ALB), glutathione aminotransferase (ALT) and glutathione aminotransferase (AST), a group of indicators of liver function, were not significantly different between PBS, E-M_{auto}@P and E-M_{allo}@P groups. Blood glucose (GLU) concentration responded to the function of the pancreas, and it did not differ between

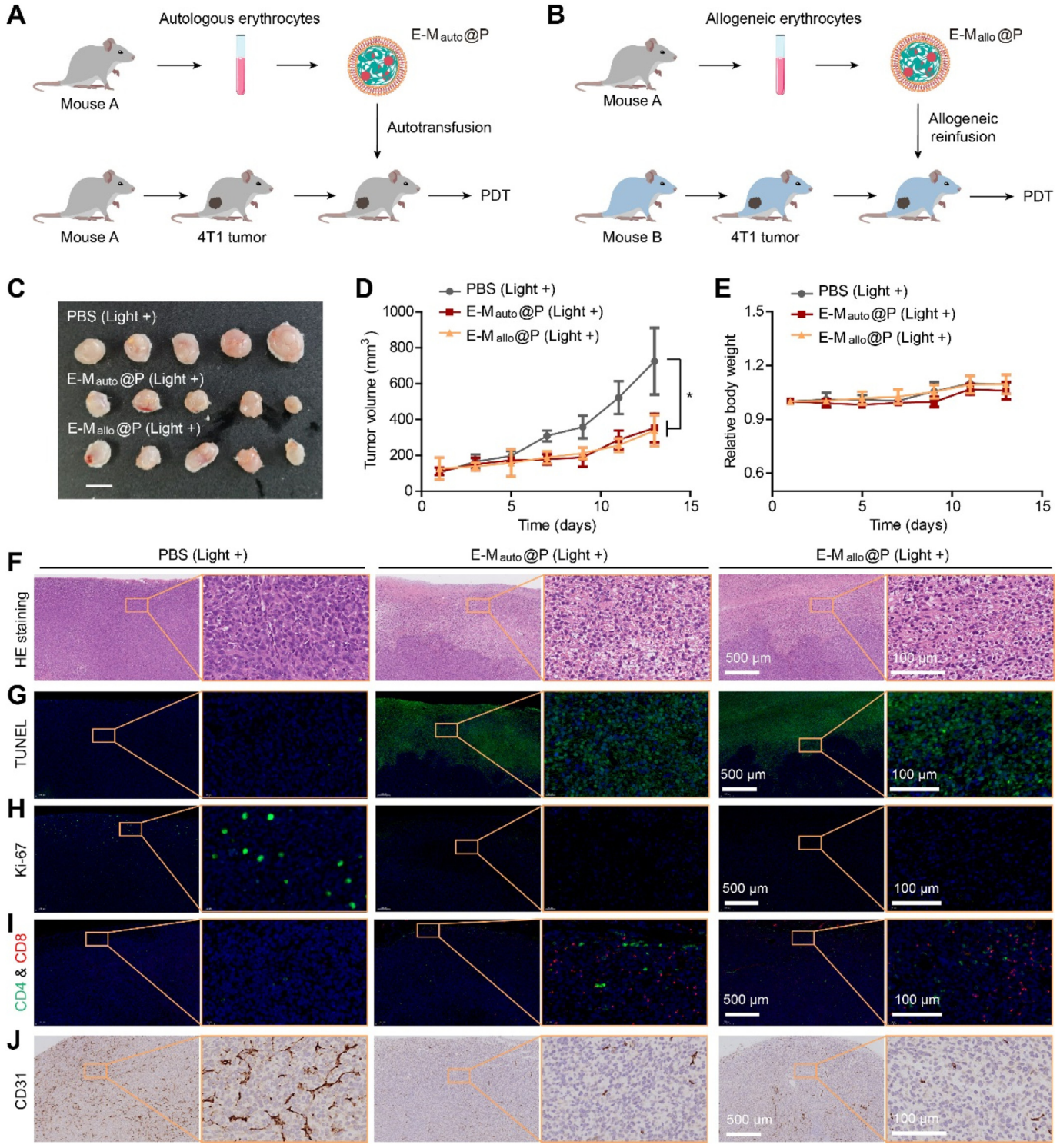

Fig. 2. E-M@P -mediated PDT against tumor growth. (A/B) Schematic diagram of the use of (A) E-M_{auto}@P or (B) E-M_{allo}@P for the treatment of tumor-bearing mice. (C) Image of tumors in tumor-bearing mice after receiving E-M_{auto}@P or E-M_{allo}@P -mediated PDT. (D) Growth kinetic curves of tumors in tumor-bearing mice after receiving E-M_{auto}@P or E-M_{allo}@P -mediated PDT (n = 5). The data were reported as mean ± SD and analyzed by unpaired *t*-test. *$p < 0.05$. (E) Relative body weight changes of tumor-bearing mice during the treatment period (n = 5). (F) HE staining, (G) TUNEL staining and (H) Ki-67 staining after the tumors received PDT. The blue channel is DAPI (Ex = 350 nm, Em = 450 nm), which is used for labeling of the nucleus. (I) Immunofluorescence staining was performed to detect the number and distribution of $CD4^+$ and $CD8^+$ cells within the tumors treated with PDT. $CD4^+$ cells are shown as green fluorescence and $CD8^+$ as red fluorescence. (J) Immunohistochemical staining to detect the number and distribution of microvessels in tumors treated with PDT.

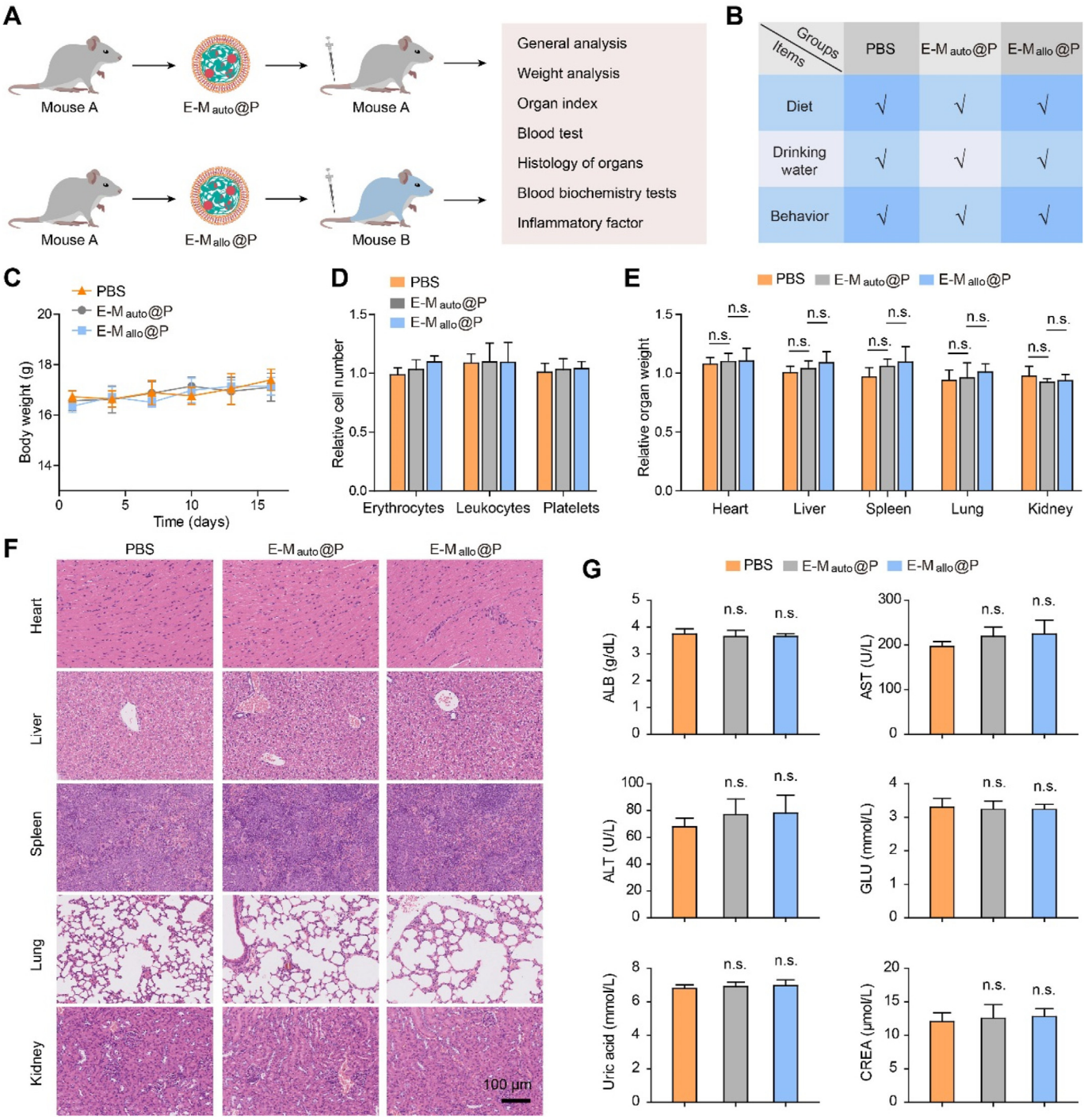

Fig. 3. Biosafety of E-M@P NPs in vivo. (A) Schematic diagram of the biosafety analysis of E-M_{auto}@P and E-M_{allo}@P in mice. (B) Changes in diet, water intake and behavior of mice after receiving different treatments (n = 3). √ indicates that the mice are eating, drinking and behaving normally. (C) Body weight changes in mice during PBS, E-M_{auto}@P and E-M_{allo}@P injections (n = 3). (D) The relative numbers of erythrocytes, leukocytes and platelets in the blood of mice treated with PBS, E-M_{auto}@P and E-M_{allo}@P, respectively (n = 3). (E) Relative weight and (F) histomorphological changes of heart, liver, spleen, kidney, lung of mice treated with PBS, E-M_{auto}@P and E-M_{allo}@P, respectively (n = 3). (G) Quantification of ALB, AST, ALT, GLU, uric acid and CREA in the blood of mice treated with PBS, E-M_{auto}@P and E-M_{allo}@P, respectively (n = 3). The data were reported as mean ± SD and analyzed by two-sided Student's t-test. *p < 0.05, **p < 0.01, ***p < 0.001, n. s. not significant.

PBS, E-M_{auto}@P and E-M_{allo}@P groups. Both uric acid and creatinine (CREA) were indicators of kidney function and they did not differ between PBS, E-M_{auto}@P and E-M_{allo}@P groups. In conclusion, this series of evaluations confirmed the biosafety of E-M@P at the overall, tissue, and molecular levels. This biosafety was not significantly different whether the NPs were prepared from autologous or allogeneic source erythrocytes.

Immune response has been an obstacle to the application of nanomedicines in vivo, not only in terms of clearance of nanomedicines by the immune system, but also in terms of causing systemic toxicities in the organism. In order to elaborate whether the erythrocyte membrane camouflaged NPs cause side effects such as immune rejection in the organism, we administered E-M_{auto}@P and E-M_{allo}@P to mice. As shown in Fig. 4A, the erythrocytes obtained from "mouse A" were prepared into

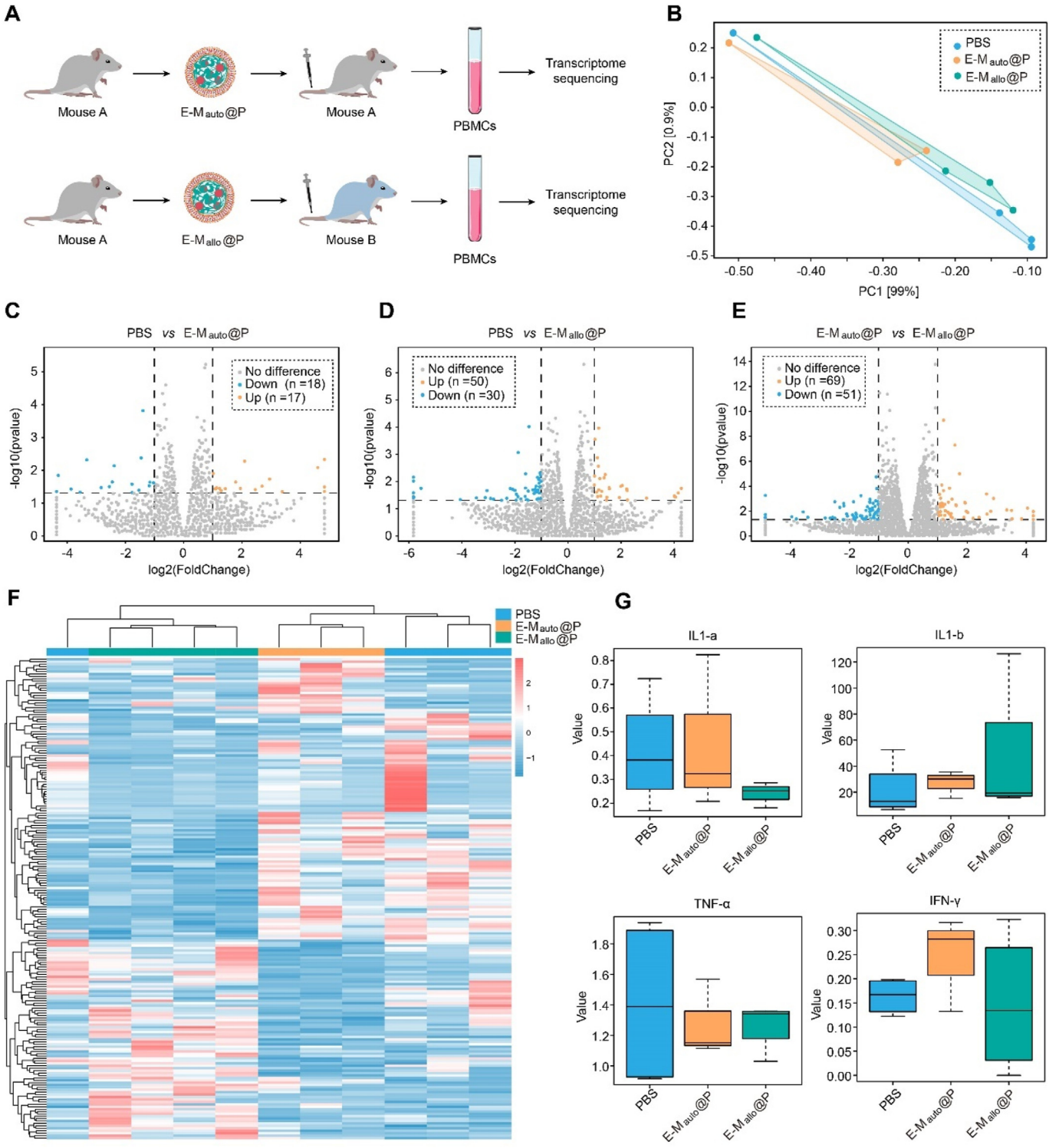

Fig. 4. Transcriptome sequencing reveals immune activation of erythrocyte membrane camouflage NPs. (A) PBMCs were isolated after auto-infusion and allogeneic infusion of erythrocyte membrane camouflaged NPs and transcriptome sequencing was performed. 4 mice in the PBS group, 4 mice in the E-M_{allo}@P group and 3 mice in the E-M_{auto}@P group. (B) Principal component analysis. (C–E) Number of significantly different genes between (C) PBS and E-M_{auto}@P, (D) PBS and E-M_{allo}@P, (E) E-M_{auto}@P and E-M_{allo}@P. (F) Heatmap of differential genes between PBS, E-M_{auto}@P and E-M_{allo}@P groups. (G) Differential analysis of IL1-a, IL-1b, TNF-α and IFN-γ between PBS, E-M_{auto}@P and E-M_{allo}@P groups.

nanoparticles and then injected back into "mouse A″, or the disguised nanoparticles of red blood cell membrane derived from "mouse A″ were injected back into "mouse B″, and finally the peripheral blood monocytes (PBMCs) in mice were isolated for transcriptome sequencing. A large amount of genetic information was obtained by transcriptome sequencing of PBMCs, aiming to analyze the changes in the state of immune cells after treatment with different NPs in mice. Principal component analysis (PCA) is a linear dimensionality reduction algorithm that is used to measure differences in data and to represent high-dimensional data with large differences by projecting them into a low-dimensional

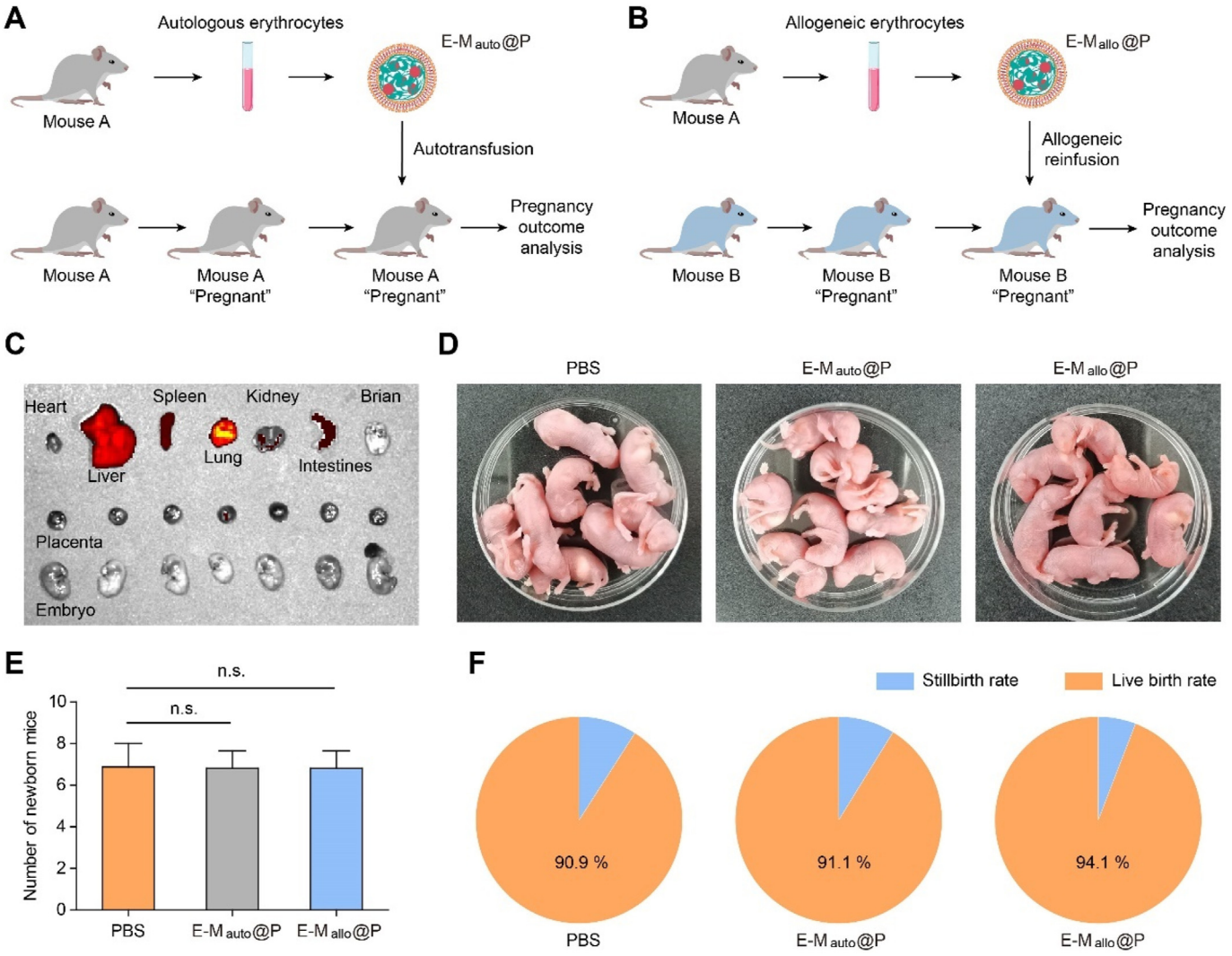

Fig. 5. Schematic diagram for assessing the safety of (A) E-M_{auto}@P and (B) E-M_{auto}@P on embryos during pregnancy. (C) IVIS assay of NPs bio-distribution after E-M@P injection into pregnant mice via tail vein. E-M@P: Ex = 500 nm, Em = 660 nm. (D/E) The litter rate of pregnant mice was observed after the injection of PBS (n = 8), E-M_{auto}@P (n = 5) and E-M_{allo}@P (n = 5) via tail vein respectively. (F) The survival rate of newborn mice was observed one week after delivery.

space. As shown in Fig. 4B, the PCA results showed no significant differences between them for either PBS, E-M_{auto}@P or E-M_{allo}@P. This means that probably neither PBS, E-M_{auto}@P nor E-M_{allo}@P had a significant activating effect on PBMCs; in short, neither E-M_{auto}@P nor E-M_{allo}@P activated the immune system. The correlation analysis showed that the correlations between the 11 samples sent for testing (4 in PBS group, 3 in E-M_{auto}@P group, 4 in E-M_{allo}@P group) were all greater than 0.85, which means that there was no significant difference between these samples (Figure S13). Further analysis revealed that 35 genes were significantly up- or down-regulated between the PBS and E-M_{auto}@P groups (Fig. 4C), and only 80 genes were significantly up- or down-regulated between the PBS and E-M_{allo}@P groups (Fig. 4D). Although 120 genes changed significantly between E-M_{auto}@P and E-M_{allo}@P, also less than 1% of the genes changed at the transcriptome level (>12,000 genes were tested) and this change can be considered small (Fig. 4E). Heatmap of the above apparently up- or down-regulated genes are shown in Fig. 4F, which showed no significant enrichment of differential genes between PBS, E-M_{auto}@P and E-M_{allo}@P groups, and the classification was not significant. In addition, individual differences between mice have to be taken into account, and even without any treatment, there will be small differences in transcriptome sequencing between them. Some important immune factors such as Interleukin 1 a (IL1-a), Interleukin 1 b (IL-1b), Tumor necrosis factor α (TNF-α) and Interferon γ (IFN-γ) were not significantly different between PBS, E-M_{auto}@P and E-M_{allo}@P groups (Fig. 4G). In conclusion, from the above sequencing results we found no significant differences in immune activation-related genes such as proliferation, activation, chemotaxis, migration, and immune factor secretion in PBMCs by either E-M_{auto}@P or E-M_{allo}@P. Therefore, it can be tentatively concluded that neither E-M_{auto}@P nor E-M_{allo}@P caused significant immune activation. However, this conclusion is only a relatively crude elaboration of the effect of erythrocyte membrane camouflaged NPs in the immune response, and further analysis of immune cell subpopulations using single cell sequencing may provide new insights.

For the safety assessment of drugs, certain special periods are also essential, such as the effects of drugs on the embryo during pregnancy. To evaluate the effect of erythrocyte membrane camouflaged NPs on embryos, healthy Balb/c mice were used to construct a pregnancy model (Fig. 5A/B). First, we investigated whether E-M@P could pass the placental barrier. Pregnant mice of approximately 14 days received NPs injections, and 24 h later the mice were dissected to isolate maternal organs, placenta, and embryonic mice. As shown in Fig. 5C, E-M@P NPs were concentrated in maternal organs, such as the liver, spleen and lungs, while the placenta and embryonic mice have almost no presence of NPs. This means that E-M@P is not able to cross the placental barrier, so it cannot reach the embryo and thus cannot directly affect it. For additional support, mice were administered E-M@P through the tail vein every 3

days from day 10 of pregnancy until delivery. In terms of litter rate, both PBS, E-M_{auto}@P and E-M_{allo}@P are similar, at about 7 per litter (Fig. 5D/E). One week after delivery, the number of surviving mice was recorded, and the live birth rates were 90.9%, 91.1%, and 94.1% for PBS, E-M_{auto}@P and E-M_{allo}@P injections, respectively (Fig. 5F). From these results, it can be inferred that the effects of erythrocyte membrane camouflaged NPs on the embryo are minimal and their application during pregnancy is promising, without caring whether the source of the erythrocyte membrane is autologous or allogeneic.

3. Conclusion

Nanomaterials, including synthetic materials and natural biomaterials, have a wide range of potential applications in medicine [72–77]. Natural biomaterials have attracted much attention in recent years due to their unique safety profile [78–80]. As one of the most widely sourced classes of natural materials, erythrocyte membranes have great promise for medical applications. Investigating the biosafety of erythrocyte membranes in vivo is a further step forward in the clinical application of cell membrane coating technology. To systemic compare whether there are differences between autologous and allogeneic erythrocyte-derived NPs in medical applications, we constructed two types of erythrocyte membrane camouflage NPs E-M_{auto}@P and E-M_{allo}@P using autologous-derived erythrocytes and allogeneic-derived erythrocytes. The erythrocyte membrane camouflaged NPs constructed by co-extrusion using AIE photosensitizer and PLGA complex as the core, which have good dispersion and stability in vitro. There was no significant difference between E-M_{auto}@P and E-M_{allo}@P in terms of tumor treatment effect assessment, they both significantly inhibited the growth of tumors. More importantly, the biosafety of erythrocyte membrane camouflage NPs was evaluated in terms of organ function, immune system, and pregnancy status. There were no differences in the functional effects on organs and minimal alterations in the immune system for either E-M_{auto}@P or E-M_{allo}@P, as well as no toxic effects on the embryo. In conclusion, it was revealed in this study that erythrocyte membrane camouflaged NPs are safe when applied in vivo, regardless of whether the NPs are prepared from autologous or allogeneic source erythrocytes. Nevertheless, this study was conducted using mice, whose blood group classification and immune system differ significantly from those of humans. Therefore, in the future, it is necessary to investigate the biosafety of erythrocyte membrane camouflage nanoparticles or autologous/allogeneic erythrocyte membrane camouflage nanoparticles for different blood groups.

Credit author statement

Dai Jun: Conceptualization, Methodology, Investigation, Formal analysis, Investigation, Data curation, Funding acquisition, Writing – original draft Chen Zhaojun: Methodology, Formal analysis, Data curation Wang Shixuan: Conceptualization Xia Fan: Funding acquisition, Project administration, Writing – review & editing Lou Xiaoding: Conceptualization, Methodology, Investigation, Investigation, Funding acquisition, Writing – review & editing, Supervision, Project administration, Funding acquisition.

Declaration of competing interest

The authors declare that they have no known competing financial interests or personal relationships that could have appeared to influence the work reported in this paper.

Acknowledgment

This work was supported by the National Key R&D Program of China (2020YFA0211200) and the National Natural Science Foundation of China (22090050, 21874121, 21974128, 52003257 and 22104040).

Appendix A. Supplementary data

Supplementary data to this article can be found online at https://doi.org/10.1016/j.mtbio.2022.100279.

References

[1] H. Pan, M. Zheng, A. Ma, L. Liu, L. Cai, Cell/Bacteria-based bioactive materials for cancer immune modulation and precision therapy, Adv. Mater. 33 (2021) 2100241, https://doi.org/10.1002/adma.202100241.
[2] M. Jurak, A.E. Wiącek, A. Ładniak, K. Przykaza, K. Szafran, What affects the biocompatibility of polymers? Adv. Colloid Interfac. 294 (2021) 102451, https://doi.org/10.1016/j.cis.2021.102451.
[3] A.S. Pitek, S.A. Jameson, F.A. Veliz, S. Shukla, N.F. Steinmetz, Serum albumin 'camouflage' of plant virus based nanoparticles prevents their antibody recognition and enhances pharmacokinetics, Biomaterials 89 (2016) 89–97, https://doi.org/10.1016/j.biomaterials.2016.02.032.
[4] B. Choi, W. Park, S. Park, W. Rhim, D.K. Han, Recent trends in cell membrane-cloaked nanoparticles for therapeutic applications, Methods 177 (2020) 2–14, https://doi.org/10.1016/j.ymeth.2019.12.004.
[5] L. Crawford, M. Wyatt, J. Bryers, B. Ratner, Biocompatibility evolves: phenomenology to toxicology to regeneration, Adv. Healthc. Mater. 10 (2021) 2002153, https://doi.org/10.1002/adhm.202002153.
[6] L. Fu, Y. Hu, C. Qi, T. He, S. Jiang, C. Jiang, J. He, J. Qu, J. Lin, P. Huang, Biodegradable Manganese-Doped calcium phosphate nanotheranostics for traceable cascade reaction-enhanced anti-tumor therapy, ACS Nano 13 (2019) 13985–13994, https://doi.org/10.1021/acsnano.9b05836.
[7] M. Xu, J. Zhu, F. Wang, Y. Xiong, Y. Wu, Q. Wang, J. Weng, Z. Zhang, W. Chen, S. Liu, Improved in vitro and in vivo biocompatibility of graphene oxide through surface modification: poly(acrylic acid)-functionalization is superior to PEGylation, ACS Nano 10 (2016) 3267–3281, https://doi.org/10.1021/acsnano.6b00539.
[8] K. Elkhoury, M. Morsink, L. Sanchez-Gonzalez, C. Kahn, A. Tamayol, E. Arab-Tehrany, Biofabrication of natural hydrogels for cardiac, neural, and bone tissue engineering applications, Bioact. Mater. 6 (2021) 3904–3923, https://doi.org/10.1016/j.bioactmat.2021.03.040.
[9] M.S. Birajdar, H. Joo, W.-G. Koh, H. Park, Natural bio-based monomers for biomedical applications: a review, Biomater. Res. 25 (2021) 8, https://doi.org/10.1186/s40824-021-00208-8.
[10] K. Joyce, G.T. Fabra, Y. Bozkurt, A. Pandit, Bioactive potential of natural biomaterials: identification, retention and assessment of biological properties, Signal Transduct. Tar. 6 (2021) 122, https://doi.org/10.1038/s41392-021-00512-8.
[11] M. Wu, W. Le, T. Mei, Y. Wang, C. Xue, Cell membrane camouflaged nanoparticles: a new biomimetic platform for cancer photothermal therapy, Int. J. Nanomed. 14 (2019) 4431–4448, https://doi.org/10.2147/ijn.s200284.
[12] X. Zhen, P. Cheng, K. Pu, Recent advances in cell membrane–camouflaged nanoparticles for cancer phototherapy, Small 15 (2019) 1804105, https://doi.org/10.1002/smll.201804105.
[13] R. Li, Y. He, S. Zhang, J. Qin, J. Wang, Cell membrane-based nanoparticles: a new biomimetic platform for tumor diagnosis and treatment, Acta Pharm. Sin. B. 8 (2018) 14–22, https://doi.org/10.1016/j.apsb.2017.11.009.
[14] B.T. Luk, L. Zhang, Cell membrane-camouflaged nanoparticles for drug delivery, J. Contr. Release 220 (2015) 600–607, https://doi.org/10.1016/j.jconrel.2015.07.019.
[15] X. Xie, X. Hu, Q. Li, M. Yin, H. Song, J. Hu, L. Wang, C. Fan, N. Chen, Unraveling Cell-type-specific targeted delivery of membrane-camouflaged nanoparticles with plasmonic imaging, Nano Lett. 20 (2020) 5228–5235, https://doi.org/10.1021/acs.nanolett.0c01503.
[16] Z. Liu, F. Wang, X. Liu, Y. Sang, L. Zhang, J. Ren, X. Qu, Cell membrane–camouflaged liposomes for tumor cell–selective glycans engineering and imaging in vivo, Proc. Natl. Acad. Sci. Unit. States Am. 118 (2021), e2022769118, https://doi.org/10.1073/pnas.2022769118.
[17] J. Li, W. Tang, Y. Yang, Q. Shen, Y. Yu, X. Wang, Y. Fu, C. Li, A programmed cell-mimicking nanoparticle driven by potato alkaloid for targeted cancer chemoimmunotherapy, Adv. Healthc. Mater. 10 (2021) 2100311, https://doi.org/10.1002/adhm.202100311.
[18] Z. Yang, D. Gao, X. Guo, L. Jin, J. Zheng, Y. Wang, S. Chen, X. Zheng, L. Zeng, M. Guo, X. Zhang, Z. Tian, Fighting immune cold and reprogramming immunosuppressive tumor microenvironment with red blood cell membrane-camouflaged nanobullets, ACS Nano 14 (2020) 17442–17457, https://doi.org/10.1021/acsnano.0c07721.
[19] Y. Bao, J. Chen, H. Qiu, C. Zhang, P. Huang, Z. Mao, W. Tong, Erythrocyte membrane-camouflaged PCN-224 nanocarriers integrated with platinum nanoparticles and glucose oxidase for enhanced tumor sonodynamic therapy and synergistic starvation therapy, ACS Appl. Mater. Interfaces 13 (2021) 24532–24542, https://doi.org/10.1021/acsami.1c05644.
[20] Y. Chen, Y. Li, J. Liu, Q. Zhu, J. Ma, X. Zhu, Erythrocyte membrane bioengineered nanoprobes via indocyanine green-directed assembly for single NIR laser-induced efficient photodynamic/photothermal theranostics, J. Contr. Release 335 (2021) 345–358, https://doi.org/10.1016/j.jconrel.2021.05.025.
[21] X. Zhang, J. Xiong, K. Wang, H. Yu, B. Sun, H. Ye, Z. Zhao, N. Wang, Y. Wang, S. Zhang, W. Zhao, H. Zhang, Z. He, C. Luo, J. Sun, Erythrocyte membrane-camouflaged carrier-free nanoassembly of FRET photosensitizer pairs with high therapeutic efficiency and high security for programmed cancer synergistic

phototherapy, Bioact. Mater. 6 (2021) 2291–2302, https://doi.org/10.1016/j.bioactmat.2021.01.004.
[22] Y. Chen, X. Shen, S. Han, T. Wang, J. Zhao, Y. He, S. Chen, S. Deng, C. Wang, J. Wang, Irradiation pretreatment enhances the therapeutic efficacy of platelet-membrane-camouflaged antitumor nanoparticles, J. Nanobiotechnol. 18 (2020) 101, https://doi.org/10.1186/s12951-020-00660-z.
[23] Q. Jiang, K. Wang, X. Zhang, B. Ouyang, H. Liu, Z. Pang, W. Yang, Platelet membrane-camouflaged magnetic nanoparticles for ferroptosis-enhanced cancer immunotherapy, Small 16 (2020) 2001704, https://doi.org/10.1002/smll.202001704.
[24] X. Cao, T. Tan, D. Zhu, H. Yu, Y. Liu, H. Zhou, Y. Jin, Q. Xia, Paclitaxel-loaded macrophage membrane camouflaged albumin nanoparticles for targeted cancer therapy, Int. J. Nanomed. 15 (2020) 1915–1928, https://doi.org/10.2147/ijn.s244849.
[25] K. Poudel, A. Banstola, M. Gautam, Z. Soe, C.D. Phung, L.M. Pham, J.-H. Jeong, H.-G. Choi, S.K. Ku, T.H. Tran, C.S. Yong, J.O. Kim, Macrophage-membrane-camouflaged disintegrable and excretable nanoconstruct for deep tumor penetration, ACS Appl. Mater. Interfaces 12 (2020) 56767–56781, https://doi.org/10.1021/acsami.0c17235.
[26] F. Jin, J. Qi, D. Liu, Y. You, G. Shu, Y. Du, J. Wang, X. Xu, X. Ying, J. Ji, Y. Du, Cancer-cell-biomimetic Upconversion nanoparticles combining chemo-photodynamic therapy and CD73 blockade for metastatic triple-negative breast cancer, J. Contr. Release 37 (2021) 90–104, https://doi.org/10.1016/j.jconrel.2021.07.021.
[27] J. Shen, J. Karges, K. Xiong, Y. Chen, L. Ji, H. Chao, Cancer cell membrane camouflaged iridium complexes functionalized black-titanium nanoparticles for hierarchical-targeted synergistic NIR-II photothermal and sonodynamic therapy, Biomaterials 275 (2021) 120979, https://doi.org/10.1016/j.biomaterials.2021.120979.
[28] Y. Fan, Y. Cui, W. Hao, M. Chen, Q. Liu, Y. Wang, M. Yang, Z. Li, W. Gong, S. Song, Y. Yang, C. Gao, Carrier-free highly drug-loaded biomimetic nanosuspensions encapsulated by cancer cell membrane based on homology and active targeting for the treatment of glioma, Bioact. Mater. 6 (2021) 4402–4414, https://doi.org/10.1016/j.bioactmat.2021.04.027.
[29] W. Xie, W.-W. Deng, M. Zan, L. Rao, G.-T. Yu, D.-M. Zhu, W.-T. Wu, B. Chen, L.-W. Ji, L. Chen, K. Liu, S.-S. Guo, H.-M. Huang, W.-F. Zhang, X. Zhao, Y. Yuan, W. Dong, Z.-J. Sun, W. Liu, Cancer cell membrane camouflaged nanoparticles to realize starvation therapy together with checkpoint blockades for enhancing cancer therapy, ACS Nano 13 (2019) 2849–2857, https://doi.org/10.1021/acsnano.8b03788.
[30] K. Zhang, X. Meng, Z. Yang, Y. Cao, Y. Cheng, D. Wang, H. Lu, Z. Shi, H. Dong, X. Zhang, Imaging of microRNA in living mice, Adv. Mater. 31 (2019) 1807888, https://doi.org/10.1002/adma.201807888.
[31] C. Yao, W. Wu, H. Tang, X. Jia, J. Tang, X. Ruan, F. Li, D.T. Leong, D. Luo, D. Yang, Self-assembly of stem cell membrane-camouflaged nanocomplex for microRNA-mediated repair of myocardial infarction injury, Biomaterials 257 (2020) 120256, https://doi.org/10.1016/j.biomaterials.2020.120256.
[32] Y. Liu, J. Zhao, J. Jiang, F. Chen, X. Fang, Doxorubicin delivered using nanoparticles camouflaged with mesenchymal stem cell membranes to treat colon cancer, Int. J. Nanomed. 15 (2020) 2873–2884, https://doi.org/10.2147/ijn.s242787.
[33] C.-M.J. Hu, L. Zhang, S. Aryal, C. Cheung, R.H. Fang, L. Zhang, Erythrocyte membrane-camouflaged polymeric nanoparticles as a biomimetic delivery platform, Proc. Natl. Acad. Sci. Unit. States Am. 108 (2011) 10980, https://doi.org/10.1073/pnas.1106634108.
[34] W. Gao, C.-M.J. Hu, R.H. Fang, B.T. Luk, J. Su, L. Zhang, Surface functionalization of gold nanoparticles with red blood cell membranes, Adv. Mater. 25 (2013) 3549–3553, https://doi.org/10.1002/adma.201300638.
[35] Y. Chen, Y. Zhang, J. Zhuang, J.H. Lee, L. Wang, R.H. Fang, W. Gao, L. Zhang, Cell-membrane-cloaked oil nanosponges enable dual-modal detoxification, ACS Nano 13 (2019) 7209–7215, https://doi.org/10.1021/acsnano.9b02773.
[36] Q. Zhang, R.H. Fang, W. Gao, L.J.A.C. Zhang, A biomimetic nanoparticle to "Lure and Kill" phospholipase A2, Angew Chem. Int. Ed. Engl. 59 (2020) 10461–10465.
[37] Y. Lian, X. Wang, P. Guo, Y. Li, F. Raza, J. Su, M. Qiu, Erythrocyte membrane-coated arsenic trioxide-loaded sodium alginate nanoparticles for tumor therapy, Pharmaceutics 12 (2020) 21, https://doi.org/10.3390/pharmaceutics12010021.
[38] Q. Pei, X. Hu, X. Zheng, S. Liu, Y. Li, X. Jing, Z. Xie, Light-activatable red blood cell membrane-camouflaged dimeric prodrug nanoparticles for synergistic photodynamic/chemotherapy, ACS Nano 12 (2018) 1630–1641, https://doi.org/10.1021/acsnano.7b08219.
[39] I. Kim, Y. Kim, S.W. Lee, D. Lee, H.G. Jung, J.W. Jang, T. Lee, Y.K. Yoon, G. Lee, D.S. Yoon, Erythrocyte-camouflaged biosensor for α-hemolysin detection, Biosens. Bioelectron. 185 (2021) 113267, https://doi.org/10.1016/j.bios.2021.113267.
[40] Z. Wang, L. Cheng, Y. Sun, X. Wei, B. Cai, L. Liao, Y. Zhang, X.-Z. Zhao, Enhanced isolation of fetal nucleated red blood cells by enythrocyte-leukocyte hybrid membrane-coated magnetic nanoparticles for noninvasive pregnant diagnostics, Anal. Chem. 93 (2021) 1033–1042, https://doi.org/10.1021/acs.analchem.0c03933.
[41] C.-M.J. Hu, R.H. Fang, J. Copp, B.T. Luk, L. Zhang, A biomimetic nanosponge that absorbs pore-forming toxins, Nat. Nanotechnol. 8 (2013) 336–340, https://doi.org/10.1073/pnas.1106634108.
[42] E. Ben-Akiva, A. Meyer Randall, H. Yu, T. Smith Jonathan, M. Pardoll Drew, J. Green Jordan, Biomimetic anisotropic polymeric nanoparticles coated with red blood cell membranes for enhanced circulation and toxin removal, Sci. Adv. 6 (2020), eaay9035, https://doi.org/10.1126/sciadv.aay9035.
[43] F. Castro, C. Martins, M.J. Silveira, R.P. Moura, C.L. Pereira, B. Sarmento, Advances on erythrocyte-mimicking nanovehicles to overcome barriers in biological microenvironments, Adv. Drug Deliv. Rev. 170 (2021) 312–339, https://doi.org/10.1016/j.addr.2020.09.001.
[44] D. Zheng, P. Yu, Z. Wei, C. Zhong, M. Wu, X. Liu, RBC membrane camouflaged semiconducting polymer nanoparticles for near-infrared photoacoustic imaging and photothermal therapy, Micro, Nano Lett. 12 (2020) 94, https://doi.org/10.1007/s40820-020-00429-x.
[45] F. Gao, Y. Tang, W.-L. Liu, M.-Z. Zou, C. Huang, C.-J. Liu, X.-Z. Zhang, Intra/extracellular lactic acid exhaustion for synergistic metabolic therapy and immunotherapy of tumors, Adv. Mater. 31 (2019) 1904639, https://doi.org/10.1002/adma.201904639.
[46] X. Han, S. Shen, Q. Fan, G. Chen, E. Archibong, G. Dotti, Z. Liu, Z. Gu, C. Wang, Red blood cell–derived nanoerythrosome for antigen delivery with enhanced cancer immunotherapy, Sci. Adv. 5 (2019), eaaw6870, https://doi.org/10.1126/sciadv.aaw6870.
[47] J. Dai, M. Wu, Q. Wang, S. Ding, X. Dong, L. Xue, Q. Zhu, J. Zhou, F. Xia, S. Wang, Y. Hong, Red blood cell membrane-camouflaged nanoparticles loaded with AIEgen and Poly(I : C) for enhanced tumoral photodynamic-immunotherapy, Natil. Sci. Rev. 8 (2021), nwab039, https://doi.org/10.1093/nsr/nwab039.
[48] X. Huang, B. Wu, J. Li, Y. Shang, W. Chen, X. Nie, R. Gui, Anti-tumour effects of red blood cell membrane-camouflaged black phosphorous quantum dots combined with chemotherapy and anti-inflammatory therapy, Artif. Cell Nanomed. Biotechnol. 47 (2019) 968–979, https://doi.org/10.1080/21691401.2019.1584110.
[49] M. Gao, C. Liang, X. Song, Q. Chen, Q. Jin, C. Wang, Z. Liu, Erythrocyte-membrane-enveloped perfluorocarbon as nanoscale Artificial red blood cells to relieve tumor hypoxia and enhance cancer radiotherapy, Adv. Mater. 29 (2017) 1701429, https://doi.org/10.1002/adma.201701429.
[50] L. Ran, B. Lu, H. Qiu, G. Zhou, J. Jiang, E. Hu, F. Dai, G. Lan, Erythrocyte membrane-camouflaged nanoworms with on-demand antibiotic release for eradicating biofilms using near-infrared irradiation, Bioact. Mater. 6 (2021) 2956–2968, https://doi.org/10.1016/j.bioactmat.2021.01.032.
[51] M. Zhang, S. Cheng, Y. Jin, N. Zhang, Y. Wang, Membrane engineering of cell membrane biomimetic nanoparticles for nanoscale therapeutics, Clin. Transl. Med. 11 (2021) e292, https://doi.org/10.1002/ctm2.292.
[52] Y. Zhai, J. Su, W. Ran, P. Zhang, Q. Yin, Z. Zhang, H. Yu, Y. Li, Preparation and application of cell membrane-camouflaged nanoparticles for cancer therapy, Theranostics 7 (2017) 2575–2592, https://doi.org/10.7150/thno.20118.
[53] S. Wang, Y. Duan, Q. Zhang, A. Komarla, H. Gong, W. Gao, L. Zhang, Drug Targeting via platelet membrane–coated nanoparticles, Small Struct 1 (2020) 2000018, https://doi.org/10.1002/sstr.202000018.
[54] X. Wu, Y. Li, F. Raza, X. Wang, S. Zhang, R. Rong, M. Qiu, J. Su, Red blood cell membrane-camouflaged tedizolid phosphate-loaded PLGA nanoparticles for bacterial-infection therapy, Pharmaceutics 13 (2021), https://doi.org/10.3390/pharmaceutics13010099.
[55] X. Que, J. Su, P. Guo, Z. Kamal, E. Xu, S. Liu, J. Chen, M. Qiu, Study on preparation, characterization and multidrug resistance reversal of red blood cell membrane-camouflaged tetrandrine-loaded PLGA nanoparticles, Drug Deliv. 26 (2019) 199–207, https://doi.org/10.1080/10717544.2019.1573861.
[56] G. Deng, X. Peng, Z. Sun, W. Zheng, J. Yu, L. Du, H. Chen, P. Gong, P. Zhang, L. Cai, B.Z. Tang, Natural-killer-cell-inspired nanorobots with aggregation-induced emission characteristics for near-infrared-II fluorescence-guided glioma theranostics, ACS Nano 14 (2020) 11452–11462, https://doi.org/10.1021/acsnano.0c03824.
[57] H. Cao, Y. Cheng, H. Gao, J. Zhuang, W. Zhang, Q. Bian, F. Wang, Y. Du, Z. Li, D. Kong, D. Ding, Y. Wang, In vivo tracking of mesenchymal stem cell-derived extracellular vesicles improving mitochondrial function in renal ischemia–reperfusion injury, ACS Nano 14 (2020) 4014–4026, https://doi.org/10.1021/acsnano.9b08207.
[58] X. Xu, G. Deng, Z. Sun, Y. Luo, J. Liu, X. Yu, Y. Zhao, P. Gong, G. Liu, P. Zhang, F. Pan, L. Cai, B.Z. Tang, A biomimetic aggregation-induced emission photosensitizer with antigen-presenting and hitchhiking function for lipid droplet targeted photodynamic immunotherapy, Adv. Mater. 33 (2021) 2102322, https://doi.org/10.1002/adma.202102322.
[59] J. Dai, X. Wu, S. Ding, X. Lou, F. Xia, S. Wang, Y. Hong, Aggregation-induced emission photosensitizers: from molecular design to photodynamic therapy, J. Med. Chem. 63 (2020) 1996–2012, https://doi.org/10.1021/acs.jmedchem.9b02014.
[60] J. Dai, X. Dong, Q. Wang, X. Lou, F. Xia, S. Wang, PEG-polymer encapsulated aggregation-induced emission nanoparticles for tumor theranostics, Adv. Healthc. Mater. 10 (2021) 2101036, https://doi.org/10.1002/adhm.202101036.
[61] Y. Wang, B. Xia, Q. Huang, T. Luo, Y. Zhang, P. Timashev, W. Guo, F. Li, X.-J. Liang, Practicable applications of aggregation-induced emission with biomedical perspective, Adv. Healthc. Mater. 10 (24) (2021) 2100945, https://doi.org/10.1002/adhm.202100945.
[62] F. Xia, J. Wu, X. Wu, Q. Hu, J. Dai, X. Lou, Modular design of peptide- or DNA-modified AIEgen probes for biosensing applications, Acc. Chem. Res. 52 (11) (2019) 3064–3074.
[63] X.L. Xu, G.J. Deng, Z.H. Sun, Y. Luo, J.K. Liu, X.H. Yu, Y. Zhao, P. Gong, G.Z. Liu, P.F. Zhang, F. Pan, L.T. Cai, B.Z. Tang, A biomimetic aggregation-induced emission photosensitizer with antigen-presenting and hitchhiking function for lipid droplet targeted photodynamic immunotherapy, Adv. Mater. 33 (2021) 2102322, https://doi.org/10.1002/adma.202102322.
[64] J. Ni, Y. Wang, H. Zhang, J.Z. Sun, B.Z. Tang, Aggregation-induced generation of reactive oxygen species: mechanism and photosensitizer construction, Molecules 26 (2021), https://doi.org/10.3390/molecules26020268.

[65] G. Feng, B. Liu, Aggregation-Induced Emission (AIE) dots: emerging theranostic nanolights, Acc. Chem. Res. 51 (2018) 1404–1414, https://doi.org/10.1021/acs.accounts.8b00060.
[66] J. Wu, Q. Wang, X. Dong, M. Xu, J. Yang, X. Yi, B. Chen, X. Dong, Y. Wang, X. Lou, F. Xia, S. Wang, J. Dai, Biocompatible AIEgen/p-glycoprotein siRNA@reduction-sensitive paclitaxel polymeric prodrug nanoparticles for overcoming chemotherapy resistance in ovarian cancer, Theranostics 11 (2021) 3710–3724, https://doi.org/10.7150/thno.53828.
[67] R.X. Li, Y.W. He, S.Y. Zhang, J. Qin, J.X. Wang, Cell membrane-based nanoparticles: a new biomimetic platform for tumor diagnosis and treatment, Acta Pharm. Sin. B. 8 (2018) 14–22, https://doi.org/10.1016/j.apsb.2017.11.009.
[68] S. He, J. Li, P. Cheng, Z. Zeng, C. Zhang, H. Duan, K. Pu, Charge-reversal polymer nano-modulators for photodynamic immunotherapy of cancer, Angew Chem. Int. Ed. Engl. 60 (2021) 19355–19363, https://doi.org/10.1002/anie.202106392.
[69] Z. Zeng, C. Zhang, J. Li, D. Cui, Y. Jiang, K. Pu, Activatable polymer nanoenzymes for photodynamic immunometabolic cancer therapy, Adv. Mater. 33 (2021) 2007247, https://doi.org/10.1002/adma.202007247.
[70] Z. Meng, X. Zhou, J. Xu, X. Han, Z. Dong, H. Wang, Y. Zhang, J. She, L. Xu, C. Wang, Z. Liu, Light-triggered in situ gelation to enable robust photodynamic-immunotherapy by repeated stimulations, Adv. Mater. 31 (2019) 1900927, https://doi.org/10.1002/adma.201900927.
[71] X. Li, J.F. Lovell, J. Yoon, X. Chen, Clinical development and potential of photothermal and photodynamic therapies for cancer, Nat. Rev. Clin. Oncol. 17 (2020) 657–674, https://doi.org/10.1038/s41571-020-0410-2.
[72] G. Chen, H. Zhang, H. Wang, F. Wang, Immune tolerance induced by immune-homeostatic particles, Eng. Regen. 2 (2021) 133–136, https://doi.org/10.1016/j.engreg.2021.09.007.
[73] L. Cai, D. Xu, H. Chen, L. Wang, Y. Zhao, Designing bioactive micro-/nanomotors for engineered regeneration, Eng. Regen. 2 (2021) 109–115, https://doi.org/10.1016/j.engreg.2021.09.003.
[74] C. Yang, Y. Yu, X. Wang, Q. Wang, L. Shang, Cellular fluidic-based vascular networks for tissue engineering, Eng. Regen. 2 (2021) 171–174, https://doi.org/10.1016/j.engreg.2021.09.006.
[75] W. Pan, Y. Tan, W. Meng, N. Huang, Y. Zhao, Z. Yu, Z. Huang, W. Zhang, B. Sun, J. Chen, Microenvironment-driven sequential ferroptosis, photodynamic therapy, and chemotherapy for targeted breast cancer therapy by a cancer-cell-membrane-coated nanoscale metal-organic framework, Biomaterials 283 (2022) 121449, https://doi.org/10.1016/j.biomaterials.2022.121449.
[76] W. Ma, Y. Yang, J. Zhu, W. Jia, T. Zhang, Z. Liu, X. Chen, Y. Lin, Biomimetic nanoerythrosome-coated aptamer–DNA tetrahedron/maytansine conjugates: pH-responsive and targeted cytotoxicity for HER2-positive breast cancer, Adv. Mater. (2022) 2109609, https://doi.org/10.1002/adma.202109609.
[77] S. Wang, M. Kai, Y. Duan, Z. Zhou, R.H. Fang, W. Gao, L. Zhang, Membrane cholesterol depletion enhances enzymatic activity of cell-membrane-coated metal-organic-framework nanoparticles, Angew. Chem. Int. Ed. (2022), e202203115, https://doi.org/10.1002/anie.202203115.
[78] W. Li, Y. Zhang, Y. Wang, Y. Ma, D. Wang, H. Li, X. Ye, F. Yin, Z. Li, Nucleic acids induced peptide-based AIE nanoparticles for fast cell imaging, Chin. Chem. Lett. 32 (2021) 1571–1574, https://doi.org/10.1016/j.cclet.2020.09.054.
[79] K. Ding, C. Zheng, L. Sun, X. Liu, Y. Yin, L. Wang, NIR light-induced tumor phototherapy using ICG delivery system based on platelet-membrane-camouflaged hollow bismuth selenide nanoparticles, Chin. Chem. Lett. 31 (2020) 1168–1172, https://doi.org/10.1016/j.cclet.2019.10.040.
[80] X. Liu, X. Zhong, C. Li, Challenges in cell membrane-camouflaged drug delivery systems: development strategies and future prospects, Chin. Chem. Lett. 32 (2021) 2347–2358, https://doi.org/10.1016/j.cclet.2021.03.015.